

Climate Impact of Cloud Water Inhomogeneity through Microphysical Processes in a Global Climate Model

HARUKA HOTTA AND KENTAROH SUZUKI

Atmosphere and Ocean Research Institute, The University of Tokyo, Kashiwa, Japan

DAISUKE GOTO

National Institute for Environmental Studies, Tsukuba, Japan

MATTHEW LEBSOCK

Jet Propulsion Laboratory, California Institute of Technology, Pasadena, California

(Manuscript received 15 October 2019, in final form 20 March 2020)

ABSTRACT


This study investigates how subgrid cloud water inhomogeneity within a grid spacing of a general circulation model (GCM) links to the global climate through precipitation processes. The effect of the cloud inhomogeneity on autoconversion rate is incorporated into the GCM as an enhancement factor using a prognostic cloud water probability density function (PDF), which is assumed to be a truncated skewed-triangle distribution based on the total water PDF originally implemented. The PDF assumption and the factor are evaluated against those obtained by global satellite observations and simulated by a global cloud-system-resolving model (GCRM). Results show that the factor implemented exerts latitudinal variations, with higher values at low latitudes, qualitatively consistent with satellite observations and the GCRM. The GCM thus validated for the subgrid cloud inhomogeneity is then used to investigate how the characteristics of the enhancement factor affect global climate through sensitivity experiments with and without the factor incorporated. The latitudinal variation of the factor is found to have a systematic impact that reduces the cloud water and the solar reflection at low latitudes in the manner that helps mitigate the too-reflective cloud bias common among GCMs over the tropical oceans. Due to the limitation of the factor arising from the PDF assumption, however, no significant impact is found in the warm rain formation process. Finally, it is shown that the functional form for the PDF in a GCM is crucial to properly characterize the observed cloud water inhomogeneity and its relationship with precipitation.

1. Introduction

The climate feedback of cloud remains one of the largest uncertainties in estimating the climate sensitivity (Boucher et al. 2013; Stephens 2005). To address this issue, realistic representations of clouds in general circulation models (GCMs) are critical. Recent advances in evaluating GCMs using satellite observations, however, have revealed that model representations of clouds are subject to systematic biases common among models,

such as geographical distributions of cloudiness and their radiative effects (Lauer and Hamilton 2013). In addition, simulated clouds potentially have “compensating biases” at their process-level characteristics in precipitation process and radiative effects even though the mean states of global climate and its long-term trend in the recent past reasonably match the observations (Kay et al. 2012; Nam et al. 2012; Stephens et al. 2010; Suzuki et al. 2013; Zhang et al. 2005). This indicates that current GCMs commonly fail to represent key underlying cloud physical processes.

The fundamental difficulty in representing clouds is rooted in the horizontal grid spacing [$O(100)$ km] adopted by modern GCMs, which is much coarser than can resolve individual clouds. This requires the models to parameterize subgrid-scale cloud processes in terms

 Denotes content that is immediately available upon publication as open access.

Corresponding author: Kentaroh Suzuki, ksuzuki@ori.u-tokyo.ac.jp

of grid-scale model variables. In particular, subgrid-scale variability of cloud liquid water content L_c (kg m^{-3}) within the cloudy part of a model grid (hereafter cloud inhomogeneity) has a significant impact on grid-scale representations of key cloud processes such as microphysics and radiative transfer process that vary nonlinearly with L_c (e.g., Pincus and Klein 2000). In general, for a nonlinear process whose rate is given as $R(L_c)$, systematic biases arise from neglecting cloud inhomogeneity and simply substituting $\overline{L_c}$ into R —that is, $R(\overline{L_c})$ —when computing $\overline{R(L_c)}$, where the overbar denotes the grid mean of in-cloud value (Larson et al. 2001).

To account for the effect of cloud inhomogeneity on $\overline{R(L_c)}$, a correction factor F that satisfies

$$\overline{R(L_c)} = F \times R(\overline{L_c}) \quad (1)$$

is often introduced into GCMs as a part of the parameterization. A typical way to introduce F is to employ a probability density function (PDF) of L_c within the grid [$P(L_c)$]. The correct estimate of $\overline{R(L_c)}$ is thus calculated as

$$\overline{R(L_c)} = \int_0^{\infty} [R(L_c) \times P(L_c)] dL_c. \quad (2)$$

This integral yields F of Eq. (1) that is determined by the nonlinearity of $R(L_c)$ and the functional form of $P(L_c)$.

Of particular importance among nonlinear processes is the autoconversion process that controls liquid-phase precipitation, exerting a substantial impact on water budget and lifetime of low-level clouds. GCMs typically treat the liquid condensates as either cloud or rain in the bulk parameterization, in which the autoconversion process accounts for conversion from cloud water into rainwater. The autoconversion rate is widely parameterized as power-law equations of L_c and cloud droplet number concentration N_c (m^{-3}) as

$$R(L_c) = -\frac{dL_c}{dt} \propto L_c^a \times N_c^{-b}, \quad (3)$$

where a and b are positive constants (Beheng 1994; Berry 1968; Khairoutdinov and Kogan 2000; Liu and Daum 2004; Tripoli and Cotton 1980). In general, the autoconversion formulation is highly nonlinear with regard to L_c ($a \gg 1$). Therefore, F in Eq. (1), termed the “enhancement factor” for the autoconversion process (hereafter denoted by E_{au}), is substantially larger than unity (Morrison and Gettelman 2008).

Due to the importance of E_{au} , it has been introduced into several GCMs. In some of these studies, E_{au} is assumed to be constant regardless of meteorological states and geographical locations (Rotstajn 2000; Morrison

and Gettelman 2008). On the other hand, observation-based studies of Barker et al. (1996) and Lebsock et al. (2013) showed that cloud water variability is greater in the trade cumulus regime than in the stratocumulus regime, suggesting that a regime-dependent representation of the cloud inhomogeneity is required in GCMs. A regime-dependent E_{au} is enabled by prognostic PDF-based parameterizations, which have been originally developed for cloud fraction diagnosis in GCMs (Tompkins 2008), based on the temporarily and spatially variant $P(L_c)$ as the saturated part of total water PDF. The prognostic PDF approach would be more theoretical than the approach that parameterizes cloud inhomogeneity as a function of cloud fraction, atmospheric stability, or convective activity (Boutle et al. 2014; Hill et al. 2015; Xie and Zhang 2015), given that PDF is a fundamental physical quantity that can also be obtained from and thus validated against observations and high-resolution cloud simulations. This approach also allows for a self-consistent treatment of cloud inhomogeneity across multiple cloud processes within a model in the way based on a common PDF.

Some studies incorporated prognostic E_{au} into the GCM and reported the improvements of cloud representations (Guo et al. 2014; Song et al. 2018a; Weber and Quaas 2012). While Hill et al. (2015) showed the impact on cloud cover and TOA radiation when parameterizing the enhancement factor for autoconversion and accretion processes, the characteristics of the factors such as their magnitude and geographical pattern were not shown, and their individual contributions were not discussed. The present study addresses a remaining question, that is, how E_{au} based on the model’s own PDF can adequately represent the global characteristics of E_{au} . We also draw on additional observations for the liquid water path (LWP) and precipitation to provide a more complete understanding of how such globally varying E_{au} with cloud regimes is linked to the global climate field.

Recent progresses in global high-resolution modeling with explicit representations of individual clouds (e.g., Satoh et al. 2019) and in global satellite observations of cloud and precipitation processes (e.g., Stephens et al. 2018) provide an unprecedented opportunity to investigate subgrid-scale characteristics of clouds and precipitation on the global scale (Lebsock et al. 2013; Hill et al. 2015). This study exploits these new capabilities to assess the fidelity of the representation of unresolved properties of cloud and their impact on nonlinear cloud processes in a GCM, taking E_{au} as a representative case that fundamentally depends on cloud inhomogeneity.

Specifically, we incorporate E_{au} into a GCM based on a prognostic PDF scheme and evaluate its global

characteristics. A detailed comparison with regard to cloud inhomogeneity representation between the GCM and global cloud-system-resolving model (GCRM) against satellite observations is then conducted for the first time to reveal the effectiveness and limitations of E_{au} parameterization based on the PDF scheme. It is revealed that the assumption for the mathematical form of cloud water PDF could be a fundamental source of bias in representing E_{au} . Given the validated characteristics of E_{au} , global climatic impacts of E_{au} are investigated through comparing GCM simulations with and without an E_{au} of varying magnitudes. The analysis is then used to explore how such process-level model characteristics relevant to the cloud inhomogeneity link to global geographical characteristics of cloud and radiation fields. The investigation of the linkage between E_{au} and warm rain process suggests a need for the E_{au} formulation to properly connect cloud inhomogeneity with precipitation. Finally, constraints inherent to a variety of mathematical functional forms for the PDF are discussed to determine the implications for other GCMs.

The rest of the paper is organized as follows: section 2 describes the experimental design to incorporate E_{au} into a GCM and the simulation setup. Section 3 provides a general description of the data and analysis methods for evaluations of the GCM-simulated cloud inhomogeneity against GCRM simulations and satellite observations. Section 4 shows the results and discussions. The main findings are summarized in section 5.

2. Global climate model simulations

a. Model description

In this study, the enhancement factor E_{au} was introduced into the atmospheric component of a GCM, the latest version of the Model for Interdisciplinary Research on Climate (MIROC6; Tatebe et al. 2019). All MIROC6 simulations in this study were conducted at a horizontal resolution of T85, which approximately corresponds to 1.4° grid spacing. The vertical resolution was 40 levels up to 3 hPa and the time step was set to 12 min.

In MIROC6, clouds and their properties are represented separately between stratiform and convective clouds as in majority of GCMs. The parameterizations most relevant to the current work are the stratiform cloud scheme. The stratiform cloud fraction (CF) and the corresponding grid-mean cloud water mixing ratio q_c (kg kg^{-1}) are derived using a statistical PDF-based scheme (Sommeria and Deardorff 1977). The scheme assumes the PDF for the conserved quantity s , denoted by $G(s)$. CF and q_c are obtained at each model grid by integrating the saturated part of $G(s)$ and $(Q_c + s)G(s)$,

respectively, where Q_c denotes the grid-scale saturation deficit. MIROC6 adopts the prognostic statistical scheme of Watanabe et al. (2009), which assumes a skewed-triangle shape for $G(s)$ as depicted in Figs. 1a–c. The shape of $G(s)$ is defined by the two prognostic variables (i.e., variance and skewness), which vary through influences by cumulus convection, cloud microphysics, turbulent mixing, and advection.

In the stratiform cloud microphysical process, grid-mean values of water vapor mixing ratio q_w , cloud water mixing ratio q_c , ice mixing ratio q_i , and cloud droplet number concentration N_c are predicted with the bulk scheme. The ice parameterization is based on Wilson and Ballard (1999). The conversion of cloud water to rainwater is computed as the sum of the autoconversion and accretion processes. Finally, N_c is predicted with the scheme of Abdul-Razzak and Ghan (2000) from aerosol number concentrations predicted by the online aerosol module, the Spectral Radiation-Transport Model for Aerosol Species (SPRINTARS; Takemura et al. 2005, 2009).

b. Incorporation of autoconversion enhancement factor

In MIROC6, autoconversion is the dominant process to produce warm rain particularly due to the diagnostic treatment of rainwater (Michibata and Takemura 2015; Michibata et al. 2019). In the current standard version of MIROC6, the autoconversion rate R_{au} ($\text{kg m}^{-3} \text{s}^{-1}$) is derived from the parameterization given by Berry (1968) (referred to herein as the BR scheme) as

$$R_{\text{au}}(L_c) = \frac{\alpha_{\text{BR}} \times L_c^2}{0.18 + 10^{-13} \times N_c / L_c}, \quad (4)$$

where α_{BR} is a “tunable” constant (Ogura et al. 2017) and L_c is the product of q_c and air density ρ_a (kg m^{-3}). In the original cloud scheme of MIROC6, the cloud inhomogeneity is not considered in the autoconversion process. The $\overline{R_{\text{au}}}$ is then calculated by simply substituting the $\overline{L_c}$ into Eq. (4) as

$$\overline{R_{\text{au}}}(L_c) = R_{\text{au}}(\overline{L_c}), \quad (5)$$

where the overbar denotes the grid mean of in-cloud value.

To incorporate the effect of the cloud inhomogeneity into the autoconversion process, we adopt the saturated part of $G(s)$ as the PDF of cloud water $P(q_c)$, as illustrated in Figs. 1a–c. Normalized $P(L_c)$ is thus obtained as

$$P(L_c) = \frac{G(s + Q_c)}{\text{CF}}, \quad (6)$$

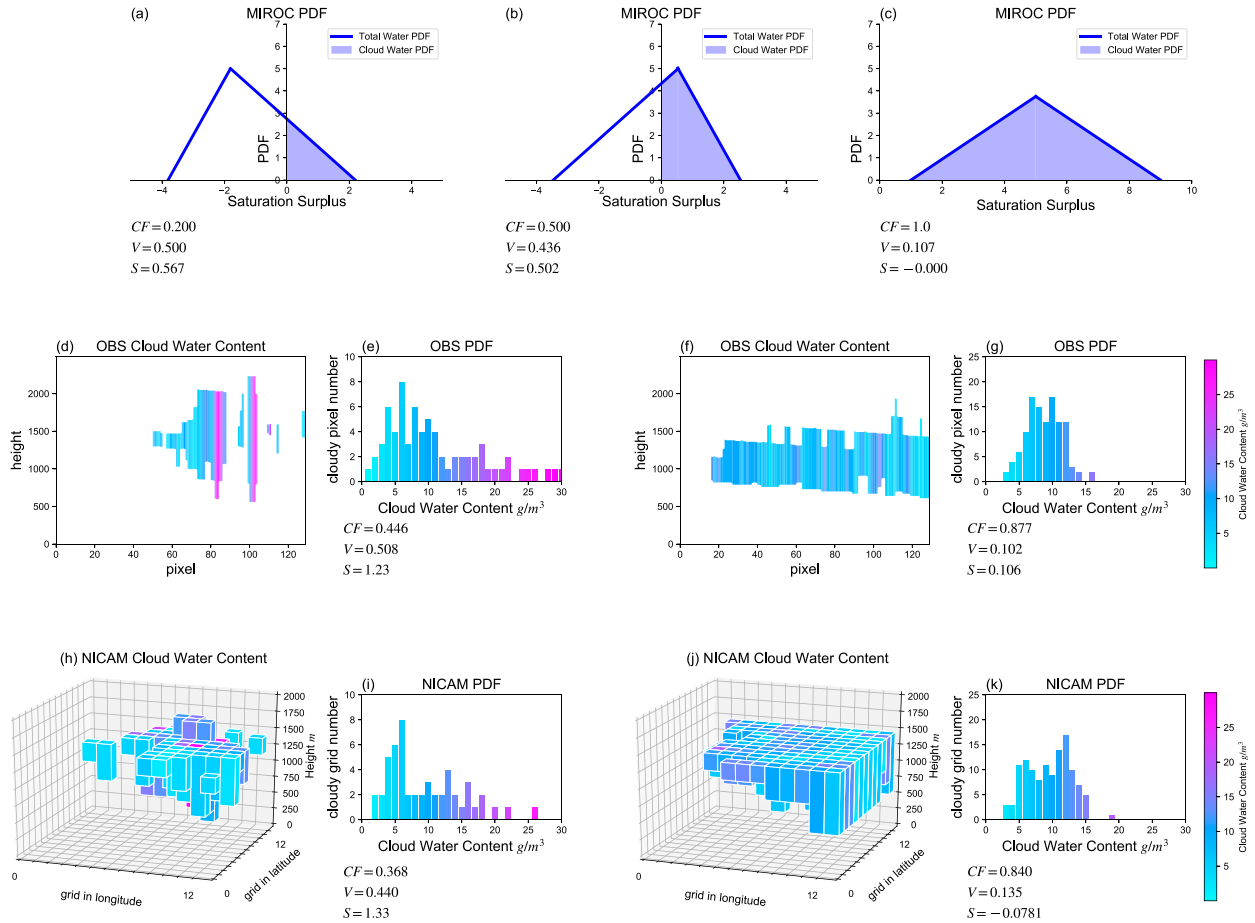


FIG. 1. Examples of cloud water PDFs (a)–(c) assumed in MIROC6, (e),(g) obtained from satellite observations, and (i),(k) constructed from the NICAM simulation. The MIROC6 figures also show the total water PDF. The saturation point (saturation surplus equals zero) corresponds to the situation that cloud water equals zero. The observed PDFs in (e) and (g) are obtained from (d),(f) the 130 sequential pixel-scale retrievals. The NICAM PDFs in (i) and (k) are from (h),(j) cloud water content at each column within the set of 144 grid points.

where $\int_0^\infty P(L_c) dL_c = 1$. Equation (4) is then integrated with weight of Eq. (6) to obtain

$$\overline{R_{\text{au}}} = \int_0^\infty [R_{\text{au}}(L_c) \times P(L_c)] dL_c. \quad (7)$$

Here the enhancement factor E_{au} is computed as

$$E_{\text{au}} = \int_0^\infty \frac{[R_{\text{au}}(L_c) \times P(L_c)]}{R_{\text{au}}(\overline{L_c})} dL_c. \quad (8)$$

The value of E_{au} depends on the shape of $P(L_c)$ and the nonlinearity of $R_{\text{au}}(L_c)$. The prognostic $P(L_c)$ allows E_{au} to be regime dependent. According to Eq. (4), the nonlinearity with regard to L_c [represented by the exponent a in Eq. (3)] of the BR scheme takes a value between 2 and 3. To explore the climate impact of E_{au} , additional simulations were conducted adopting autoconversion schemes that have different nonlinear

exponents, namely the schemes of [Khairoutdinov and Kogan \(2000\)](#) and [Beheng \(1994\)](#) (hereafter the KK and BH schemes, respectively). The conversion rates for the KK and BH schemes are given by

$$R_{\text{au}}(L_c) = \alpha_{\text{KK}} \times 1350 L_c^{2.47} (N_c \times 10^{-6})^{-1.79} \rho_\alpha^{-1.47}, \quad (9)$$

and

$$R_{\text{au}}(L_c) = \alpha_{\text{BH}} \times 6.0 \times 10^{28} (L_c \times 10^{-3})^{4.7} (N_c \times 10^{-6})^{-3.3}, \quad (10)$$

respectively, where α_{KK} and α_{BH} are “tunable” constants. These schemes have the nonlinearity of $a = 2.47$ and 4.7 in Eq. (3). The BH scheme is characterized by remarkably higher nonlinearity. For some PDF shapes previously adopted in GCMs, the cloud water PDF need to be assumed in the way inconsistent with total water PDF ([Guo et al. 2014](#); [Song et al. 2018a](#)) or to be

numerically integrated, which requires expensive computational cost (Weber and Quaas 2012). In contrast, integrations of Eq. (8) were conducted analytically for all the three autoconversion formulations because $P(L_c)$ in this study is a linear function.

c. Experimental design

In addition to the control (Cont) experiments that neglect cloud inhomogeneity when evaluating $\overline{R_{au}}$ [as in Eq. (5)], two different types of experiments, denoted as the E_{au} and E_{au} -tune experiments, were conducted for each of the three alternate autoconversion schemes. In the E_{au} experiments, E_{au} was introduced according to Eq. (8). This imposed a feedback onto liquid cloud distribution and thus had an impact on the radiation field. In the E_{au} -tune experiment, the coefficient parameters (α_{BR} , α_{KK} , and α_{BH}) were retuned to maintain the global and annual average net TOA radiation balance within $\pm 1 \text{ W m}^{-2}$ in addition to the introduction of E_{au} .

As a result of the experimental setup described above, the total of nine experiments (Cont, E_{au} , and E_{au} -tune for three choices of autoconversion schemes) were conducted with MIROC6. The simulation period was 4 years for each experiment. Observed monthly mean sea surface temperature and sea ice data of the year 2005–08 were used as boundary conditions. The concentrations of anthropogenic gases and aerosols were set to present-day emissions. The simulated results were analyzed to show the mean state of the last three years unless otherwise stated.

d. COSP

To facilitate the quantitative evaluation of clouds in MIROC6 against satellite observations, we used the satellite simulator COSP version 1.4 (Bodas-Salcedo et al. 2011). In this study, low-level ($>680 \text{ hPa}$) CF of MIROC6 diagnosed by the COSP lidar module was evaluated against CALIPSO remote sensing using the GCM-Oriented CALIPSO Cloud Product (GOCCP; Chepfer et al. 2008, 2010; Guzman et al. 2017) algorithm. In addition, we evaluated the warm rain characteristics in MIROC6 through comparisons of radar reflectivity statistics from COSP radar simulator (Haynes et al. 2007) with CloudSat observations (Stephens et al. 2008).

The online COSP diagnostics were conducted every 3 h in the MIROC6 integrations. The number of subcolumns generated in each grid was 140. The stratiform cloud water and rainwater were assumed to uniformly distribute within the stratiform cloud subcolumns in the grid box. This assumption possibly causes overestimated radar reflectivity (Song et al. 2018b; Hillman et al. 2018), which will be discussed

later (section 4d). The maximum-random cloud overlap assumption was applied in the vertical cloud assignment.

3. Method to analyze cloud inhomogeneity

Figure 1 displays examples of the cloud water PDF $P(L_c)$ that is 1) assumed in the GCM MIROC6 PDF-based cloud parameterizations (Figs. 1a–c), 2) obtained from pixel-scale observations by satellites (Figs. 1e,g), and 3) simulated by the GCRM NICAM with its fine grids (Figs. 1i,k) by the method described below. For the comparisons, we characterized cloud inhomogeneity in terms of dimensionless parameters, that is, normalized variance V (the arithmetic variance divided by the square of mean) and skewness S . Mathematically defined as $\left[\int_0^\infty (L_c - \overline{L_c})^2 P(L_c) dL_c \right] / \overline{L_c}^2$, V is a measure of cloud water variability, with its large values indicating more heterogeneous cloud field. The V and equivalent variables have been widely analyzed observationally and often chosen to specify cloud inhomogeneity within a GCM grid (e.g., Guo et al. 2014; Hill et al. 2012; Shonk et al. 2010) with its impact on cloud processes via the enhancement factors (e.g., Kawai and Teixeira 2012; Lebsock et al. 2013). The subgrid-scale variability of N_c is also likely to enhance the autoconversion rate over regions with large N_c , particularly for autoconversion schemes with the exponent b in Eq. (3) significantly larger than unity such as in the KK and BH schemes (Wu et al. 2018; Zhang et al. 2019). However, this study assumes a uniform distribution of N_c given that there seems no reliable parameterization for N_c variability partly due to the quite limited observations for N_c variability. The analysis was focused on oceanic single-layer warm clouds, whose cloud-top temperatures are higher than 273.15 K.

a. Satellite analysis

1) THE DATA

For observation-based evaluations of the cloud inhomogeneity and its impact on precipitation on the global scale, we exploited the measurements from the A-Train satellite constellation (Stephens et al. 2002) over a 4-yr period (2007–10), which covers from 82°S to 82°N with its sun-synchronous polar orbit. The analysis is based on the method of Lebsock et al. (2013). We employed data from the CloudSat Cloud Profiling Radar (CPR), CALIPSO CALIOP lidar, and MODIS instrument on Aqua. These three satellites fly as part of the A-Train. We used pixel-level data from the CPR footprint size of about 1.7 km in the horizontal, with an along-track

sampling interval of 1.1 km and at a vertical resolution of 240 m.

The LWP and N_c were derived from the MODIS collection 5.1 level 2 MYD06 of optical thickness τ and effective particle radius R_e retrieved by the 2.1- μm channel (Platnick et al. 2003). Using an adiabatic assumption with constant N_c in height (Wood 2006), LWP was estimated as $\text{LWP} = (5/9)\tau R_e \rho_w$, where ρ_w denotes the liquid water density. The value of N_c was estimated as $N_c = \sqrt{2}B^3\Gamma_{\text{eff}}^{1/2}$, where $B = 0.0620 \text{ kg}^{-1/3} \text{ m}$, and Γ_{eff} is the effective rate of increase in liquid water content with respect to height. The analysis was limited to the ascending (sunlit) orbits that cross the equator at approximately 1330 local time, when the retrievals are available. The cloud geometric thickness H was taken from the combined radar/lidar cloud mask provided in the 2B-GEOPROF-lidar P2 R04 product (Mace et al. 2009). We note that the uncertainty of cloud-base height would not be crucial for the horizontal cloud inhomogeneity analysis (Lebsock et al. 2013), although in some cases the cloud layer near surface is possibly undetected, causing underestimated H .

2) ANALYSIS METHOD

Sequences of 130 continuous profiles (corresponding to the MIROC6 horizontal grid size of approximately 140 km) were extracted from the CPR granules to define a segment of satellite data. Cloudy pixels were defined as those that satisfy the radar/lidar cloud mask and also have successful retrievals of τ and R_e . A sample was discarded if the multilayer cloud flag by the radar/lidar cloud mask was contained or if any cloudy pixel possesses a cloud-top temperature lower than 273.15 K. The remaining segments are therefore composed of clear-sky and single-layer warm cloud pixels. Segments containing more than two valid cloud retrieval pixels were required so that S has a meaningful value. For each cloudy pixel, L_c was simply estimated as $L_c = \text{LWP}/H$.

For each segment, V and S were calculated using the method of moments. The value of N_c was averaged within the cloudy pixels and then the value of E_{au} was evaluated assuming the autoconversion to be either of the three schemes. The cloud fraction was defined as the ratio of the cloudy pixel number relative to 130.

For evaluations of warm rain, the radar reflectivity Z_e (expressed in dBZ) from the 2B-GEOPROF-lidar product was employed. The higher Z_e is typically associated with greater likelihood of precipitation. The lowest four pixels (1 km above the surface) of Z_e were discarded to avoid the ground clutter following Tanelli et al. (2008).

b. GCRM analysis

1) MODEL AND SIMULATION SET UP

The 1-yr simulations with Nonhydrostatic Icosahedral Atmospheric Model (NICAM) (Satoh et al. 2008, 2014; Suzuki et al. 2008; Tomita and Satoh 2004), which were also used in Sato et al. (2018), were analyzed. The horizontal resolution employed was approximately 14 km (grid division level 9). The vertical grid was 38 levels extending to the height of 40 km above the sea level, and the time step was set to 1 min.

NICAM dynamics employs a set of governing equations for a fully compressive fluid on the icosahedral grids. Cloud microphysics adopted a one-moment bulk scheme called NICAM single-moment water 6 (NSW6; Tomita 2008), and no cumulus parameterization was applied. In NSW6, the mixing ratios of water vapor q_v , cloud q_c , rain q_r , ice q_i , snow q_s , and graupel q_g are predicted based on microphysical conversion processes, and saturation adjustment is applied between q_v and q_c ; N_c is predicted by the scheme of Abdul-Razzak and Ghan (2000) in online SPRINTARS.

The numerical integrations were conducted with sea surface temperature prescribed for the 20-yr average results of Kodama et al. (2015) after spinup periods of 1.5 months. Two types of simulations, which adopted the BR and KK schemes for the autoconversion process respectively, were analyzed. For warm rain evaluations, the Joint Simulator for Satellite Sensors (J-simulator; Hashino et al. 2013) was applied to the NICAM-simulated atmosphere profiles. The J-simulator calculated the attenuated radar reflectivity at 94 GHz at a horizontal resolution of 14 km.

2) ANALYSIS METHOD

Using the 6-hourly instantaneous output at 14-km grid spacing, we analyzed the cloud inhomogeneity within a grid size of MIROC6, which consists of 144 horizontal points of the NICAM output (12 pixels in longitude and latitude, respectively). We extracted the sets of points composed of single-layer warm cloud columns and clear-sky columns alone. A volume (a grid point at a vertical level) was assumed as cloudy if the sum of the hydrometeor condensate mixing ratio ($q_c + q_r + q_i + q_s + q_g$) in the volume exceeds the threshold chosen to be $10^{-5} \text{ kg kg}^{-1}$. As a result, cloudy columns are selected as those that satisfy all the following three conditions: 1) liquid-phase condensate mixing ratio ($q_c + q_r$) $\geq 10^{-5} \text{ kg kg}^{-1}$ from cloud-top layer to cloud-bottom layer, 2) cloud-top temperature $\geq 273.15 \text{ K}$, and 3) cloud optical thickness ≥ 0.3 . Clear-sky columns are defined as those that satisfy either or

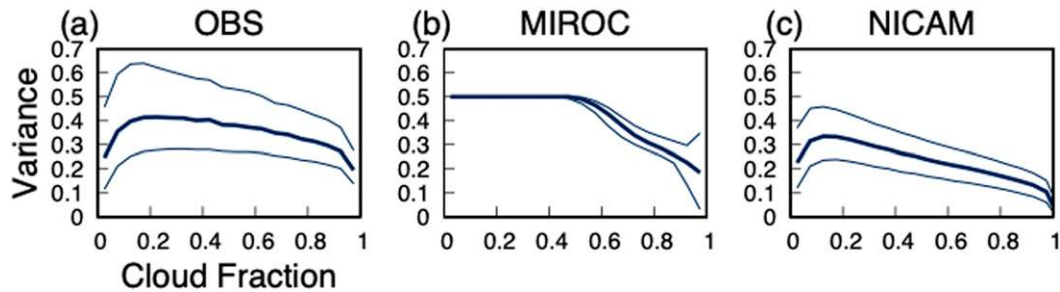


FIG. 2. Normalized variance V of cloud water content for warm clouds as a function of cloud fraction in (a) satellite observations, (b) MIROC6, and (c) NICAM. The bold lines show the median, and thin lines show the 25th and 75th percentiles.

both of the following two conditions: 1) none of the layer is cloudy and 2) cloud optical thickness ≤ 0.3 .

For a selected cloudy column, the LWP contained within the whole layer (including clear-sky layer) was divided by the H to obtain L_c as LWP/ H in the manner consistent with satellite analysis. The CF is defined as the fractional count of cloudy columns relative to 144.

3) MIROC6 ANALYSIS

Cloud inhomogeneity parameters in MIROC6 simulations were analyzed with the instantaneous output data at 6-hourly intervals. A column was selected if the conditions 1–3 above for NICAM cloudy column were satisfied, where the hydrometer condensate mixing ratio was replaced with the sum of q_c and q_i in MIROC6. For each cloudy volume (at a level within a column), CF, V , S , and E_{au} are obtained by analytical calculation using $P(L_c)$ of the volume. These variables were vertically averaged within cloudy layers weighted with L_c of each layer.

4. Results and discussion

a. Cloud inhomogeneity

The cloud inhomogeneity in MIROC6 is at first compared with that in satellite observations and NICAM. We note that the horizontal resolution of 14 km adopted by NICAM is substantially larger than that of satellite retrieval pixels. NICAM thus cannot completely capture the cloud inhomogeneity as small as those captured by satellite measurement. However, NICAM even at this resolution is one of the most elaborate models that enable year-long and global-scale experiments under current computational capability. We therefore regard NICAM as a superior model to traditional GCMs in terms of cloud inhomogeneity representations.

It should also be noted that the absolute value of CF and cloud inhomogeneity parameters are subject to

analysis conditions such as water mixing ratio threshold that distinguishes cloudy and clear-sky conditions and the horizontal scale of sampling the data (Boutle et al. 2014; Hill et al. 2012; Lebsock et al. 2013). Given that it is impossible to make these conditions exactly identical between MIROC6, NICAM, and satellite observations, we focus on qualitative comparisons of the cloud inhomogeneity. In this subsection, we show results from the MIROC6 E_{au} -tune experiment and NICAM both with the BR scheme for evaluating the models.

A primary factor controlling cloud inhomogeneity is CF, as found by prior observational analysis (Ahlgren and Forbes 2016; Boutle et al. 2014; Hill et al. 2012; Lebsock et al. 2013; Xie and Zhang 2015). Figure 2 compares how V is correlated with CF in MIROC6, satellite observations, and NICAM. Satellite observations show that V tends to increase and decrease with increasing CF when the CF is smaller and larger than about 0.2, respectively. The bell-shaped relationship, similar to what is found in the previous studies, is well reproduced in NICAM at least qualitatively. This suggests that explicit representations of the cloud inhomogeneity in NICAM with fine grids (Figs. 1d,f) can capture the satellite-observed subgrid-scale water variability characteristics. In MIROC6, on the contrary, V almost takes a single value of 0.500 when CF is smaller than 0.5. In this situation, $P(L_c)$ is fixed to be a right-angled triangular shape (Fig. 1a) and unable to form other shapes such as the distribution with the long tail toward high liquid water content (Figs. 1e,i), resulting in the confined value of $V = 0.5$. The cloud inhomogeneity of MIROC6 is thus overconstrained by CF, particularly over small CF conditions, due to the skewed-triangle shape $G(s)$ assumed. For CF larger than 0.5, although the variability at a given CF is small, V in MIROC6 decreases as CF increases, which is consistent with satellite observations and NICAM.

The correlation characteristics are also found in the context of global geographical distributions of V and

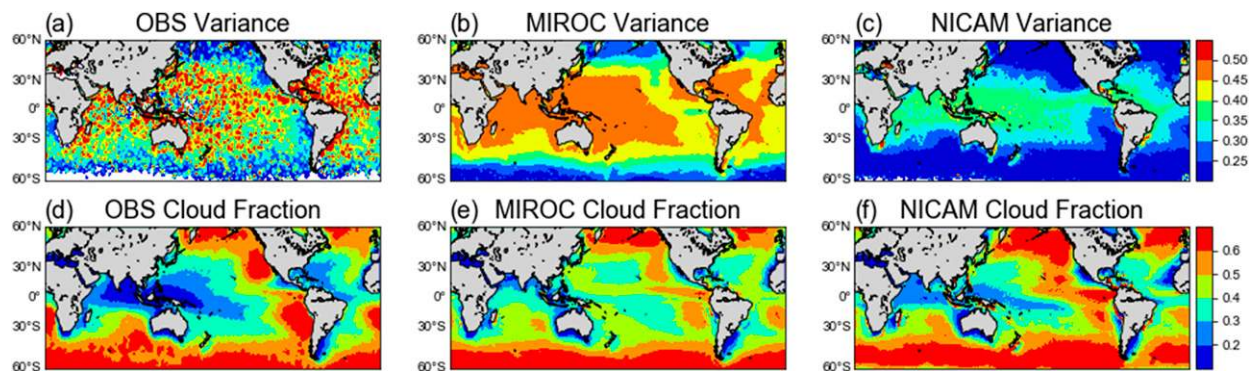


FIG. 3. Mean value of cloud water normalized variance V for warm clouds in (a) satellite observations, (b) MIROC6, and (c) NICAM. Climatological of low-level (>680 hPa) cloud fractions are derived by (d) the *CALIPSO* GOCCP version 3 algorithm in *CALIPSO* satellite observations for the years 2007–10 and (e) the MIROC-COSP lidar simulator. The low-level cloud fraction of NICAM is constructed from 6-hourly instantaneous diagnosis: For each column, low-level cloud fraction is assigned as 1 if any layer below 680 hPa is cloudy and as 0 otherwise. (f) The annual mean value.

low-level CF as shown in Fig. 3. In satellite observations (Fig. 3a), the region of low (high) V well corresponds to where low-level clouds are ubiquitous (sparse). This implies that the meteorological conditions associated with CF play a crucial role in determining the geographical distribution of V through the relationship of Fig. 2a. The low values of V are observed particularly over high latitudes and on the eastern margins of the subtropical ocean basins, where stratus and stratocumulus are the principal cloud types. In contrast, high values of V are observed in the tropical central ocean, where trade wind cumulus clouds typically occur and $P(L_c)$ is often characterized by a long tail extending toward large L_c (Fig. 1e). These regional characteristics are captured by NICAM quite well (Fig. 3c). MIROC6 reproduces the latitudinal variation of V , with detailed regional characteristics of V found to be biased (Fig. 3b). In the eastern margin of subtropical oceans, for example, the locations with low V is shifted to the west in MIROC6, which is likely related to the CF bias that stratocumulus region is too far from the coast (Fig. 3d).

b. Enhancement factor for autoconversion

The characteristics of the cloud inhomogeneity influence the process rate as an enhancement factor through Eq. (2) with an assumed functional form of $P(L_c)$ in GCMs (Kawai and Teixeira 2012). Given that the mathematical form of $P(L_c)$ serves as a “closure” that connects the lower and higher moments of the cloud water distribution, it would be helpful to investigate the relationship among different statistical properties of cloud water PDF such as V and S and their link to E_{au} for understanding how prescribed form of PDFs captures and possibly constrains the relationships in representing the enhancement factor.

Figures 4a–c illustrate the statistical relationship between V and S in the form of the joint PDFs, which characterizes the “shape” of $P(L_c)$ as illustrated in Figs. 4d–f. Satellite observations (Fig. 4a) show that V and S tend to be positively correlated with each other, which is successfully simulated by NICAM (Fig. 4c), suggesting that key observed characteristics of $P(L_c)$ are well captured by NICAM. The relatively rare occurrence of positively skewed distribution in NICAM might be because NICAM lacks shallow cumulus clouds, which is not expected to be fully resolved with 14-km horizontal resolution. On the other hand, this relationship in MIROC6 is strongly constrained by the assumption that $G(s)$ is a skewed triangle. In particular, 69% of the analyzed column corresponds to a single point (green dot in Fig. 4b), where $V = 0.500$ and $S = 0.567$ with a right-angled triangle $P(L_c)$ in Fig. 1a. Figure 4b also shows that the MIROC6 cloud scheme restricts the range of V and S to $0 \leq V \leq 0.500$ and $-0.567 \leq S \leq 0.567$.

Figure 5 demonstrates how V and S influence the value of E_{au} for different choices of autoconversion schemes. It is found that E_{au} is largely determined by V in the case of the BR and KK schemes, while both V and S have comparable contributions to E_{au} for the BH scheme because of its higher nonlinearity for L_c . These results illustrate how limited variations of V and S in MIROC6 (Fig. 4b) prevent E_{au} from taking large values. It is therefore suggested that the skewed-triangle shape assumption for $G(s)$ in MIROC6 is a fundamental source of bias in parameterizing E_{au} , particularly for conditions of large cloud inhomogeneity.

The global geographical distributions of E_{au} are shown in Fig. 6. As expected from the close relations of E_{au} with V in Fig. 5, the regional variations of E_{au} reflect

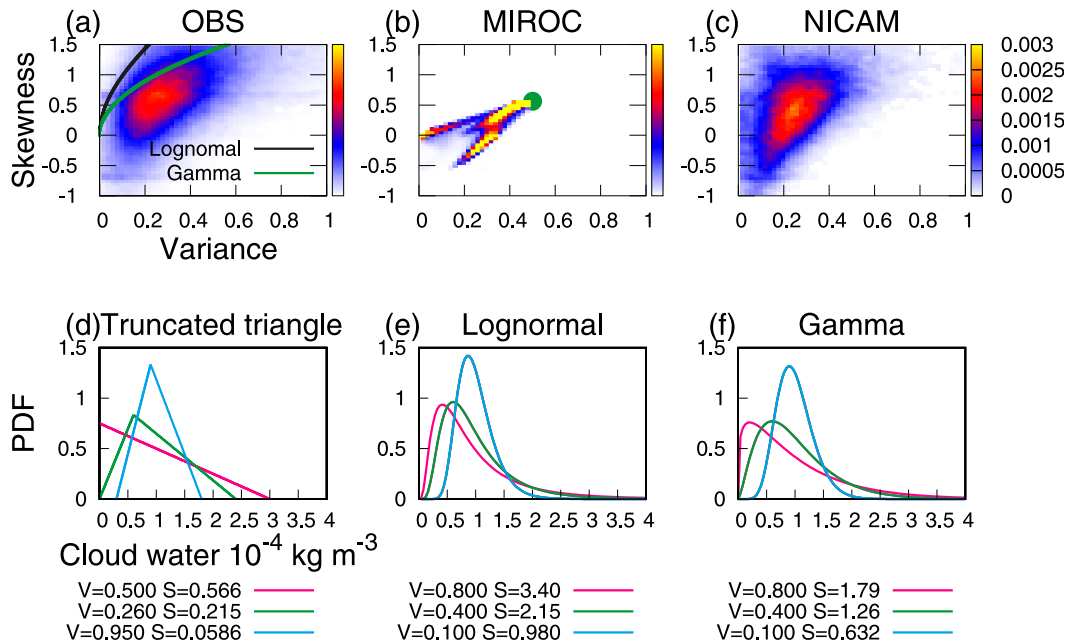


FIG. 4. Characteristics of cloud water PDF represented with its cloud water normalized variance V and skewness S . The fractional occurrence of V (abscissa) and S (ordinate) is shown for (a) satellite observations, (b) MIROC6, and (c) NICAM. The numbers of bins for normalized V and S are 50. The relationships of V and S are plotted by the black line (lognormal distribution) and by the green line (gamma distribution), respectively in (a). The green dot shown in (b) corresponds to the point where V equals 0.500 and S equals 0.567. Examples of cloud water PDFs are shown with their values of V and S for (d) the truncated skewed triangle as in MIROC6 assumption, (e) lognormal distribution, and (f) gamma distribution. All the PDFs are normalized, and their mean values are adjusted to $1.0 (10^{-4} \text{ kg m}^{-3})$.

those of V shown in Fig. 3. The E_{au} takes relatively low values at the high latitudes and on the eastern margin of the subtropical oceans similar to V in satellite observations. As expected, the BH scheme has the largest value of E_{au} , reflecting the highest nonlinearity. In addition, the BH case does not show as clear longitudinal variation as the BR and KK scheme cases at subtropical oceans, likely reflecting the strong dependence of E_{au} on S as well as on V . MIROC6 represents the E_{au} characteristics differently from satellite observation and NICAM over subtropical oceans: The distribution is rather uniform zonally and the particularly high E_{au} values in convective cloud regimes are missing. These biases are interpreted to arise from the MIROC6 parameterization that overconstrain the E_{au} values at low CF regime as argued above. The latitudinal variation with larger E_{au} values at low latitudes in MIROC6, however, is consistent with those of satellite observations and NICAM.

c. Impact of enhancement factor on global cloud field

To assess the climatic impact of E_{au} , the mean states of the cloud properties and their responses to the E_{au} in MIROC6 simulations are investigated. Since the auto-conversion process serves as a sink for cloud water, its

modification with E_{au} would directly impact LWP. The simulated LWP climatology is thus evaluated against the Multisensor Advanced Climatology of LWP (MAC-LWP; Elsaesser et al. 2017) datasets, which provide satellite-based monthly oceanic LWP. Figure 7 compares LWP of the observation (Fig. 7a), model biases of the Cont experiments (Cont minus observation; Figs. 7c,f,i), and the impacts of E_{au} with and without retuning ($E_{\text{au-tune}}$ minus Cont and E_{au} minus Cont; Figs. 7e,h,k,d,g,j).

In the E_{au} experiments, LWP is overall reduced due to the enhanced conversion from cloud water to rainwater. The BH case shows the largest decrease due to the highest value of E_{au} (Fig. 6). In the $E_{\text{au-tune}}$ experiments, this reduction of LWP is compensated for by the increase of cloud water induced by retuning of the α coefficient. This competition between E_{au} and retuning shapes the regional variations of the LWP response shown in Figs. 7e, 7h, and 7k. These figures, together with Fig. 6, illustrate that LWPs generally increase at higher latitudes where E_{au} is relatively small, whereas LWPs are rather reduced at tropical ocean where E_{au} is large. The responses of low-level CF tend to correspond to those of LWP, although their geographical distributions are rather noisy: E_{au} overall reduced CF and $E_{\text{au-tune}}$ tended to reduce CF at low latitudes (not shown).

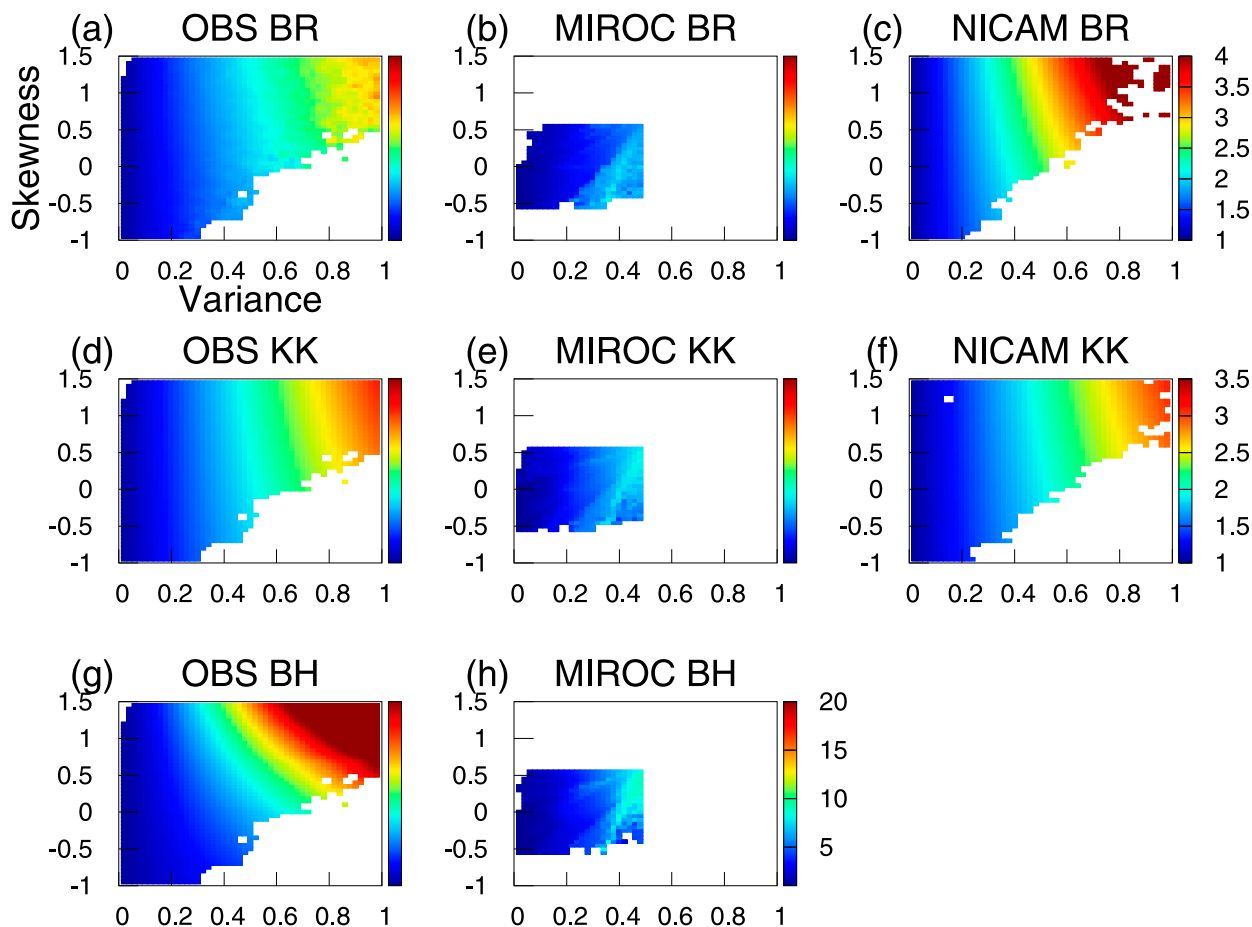


FIG. 5. Mean value of factor E_{au} as a function of cloud water normalized variance (abscissa) and skewness (coordinate) in (left) satellite observations, (center) MIROC6, and (right) NICAM for the (a)–(c) BR, (d)–(f) KK, and (g), (h) BH autoconversion schemes. The range of the color bar is the same for each row.

These responses of cloud fields are expected to have a significant impact on the radiation field in MIROC6. The geographical distributions of shortwave cloud radiative effect (SWCRE) at TOA is evaluated against the data of CERES-EBAF at TOA edition 4.0 (Loeb et al. 2018) in Fig. 8. The response of SWCRE in the MIROC6 E_{au} experiments (Figs. 8c,f,i) and E_{au} -tune experiments (Figs. 8d,g,j) affirm that the geographical distribution of E_{au} systematically influences the SWCRE distribution. In the E_{au} experiments, SWCRE is generally decreased with the BH case exerting the largest decrease reflecting the highest value of E_{au} . The E_{au} -tune experiment exhibits latitudinal characteristics that SWCRE tends to be larger (rendering the region warmer) over tropical oceans while SWCRE appears to decrease (cooler effect) at high latitudes.

Based on the characteristics of E_{au} over oceans and their global effects described above, let us argue whether the incorporation of E_{au} could help mitigate the cloud biases typical among GCMs. For this purpose, the

Cont and E_{au} -tune MIROC6 results are compared and the impacts of E_{au} on cloud and radiation fields shown above are discussed here. First, we note that the amplitude of E_{au} in MIROC6 is restricted particularly for the convective cloud regime due to the constraint of PDF assumption (Fig. 5). This is likely to limit the impact of E_{au} on the climate field in MIROC. However, the BH experiment with largest variability of E_{au} (Fig. 6h) would overcome the limitation regarding the absolute magnitude of the E_{au} effect and would exert the most pronounced impact on climate among the three autoconversion schemes tested. Figure 7 indicates that LWP responses to E_{au} , particularly with retuning, do not necessarily reduce the LWP biases and even tend to worsen the LWP bias, especially at high latitudes. We note that the LWP responses are comparable to uncertainty in satellite retrieval of LWP (Fig. 7b), implying that cloud responses induced by E_{au} may not be large enough to be fully validated with satellite observations. Focusing on SWCRE, nevertheless, the too-reflective

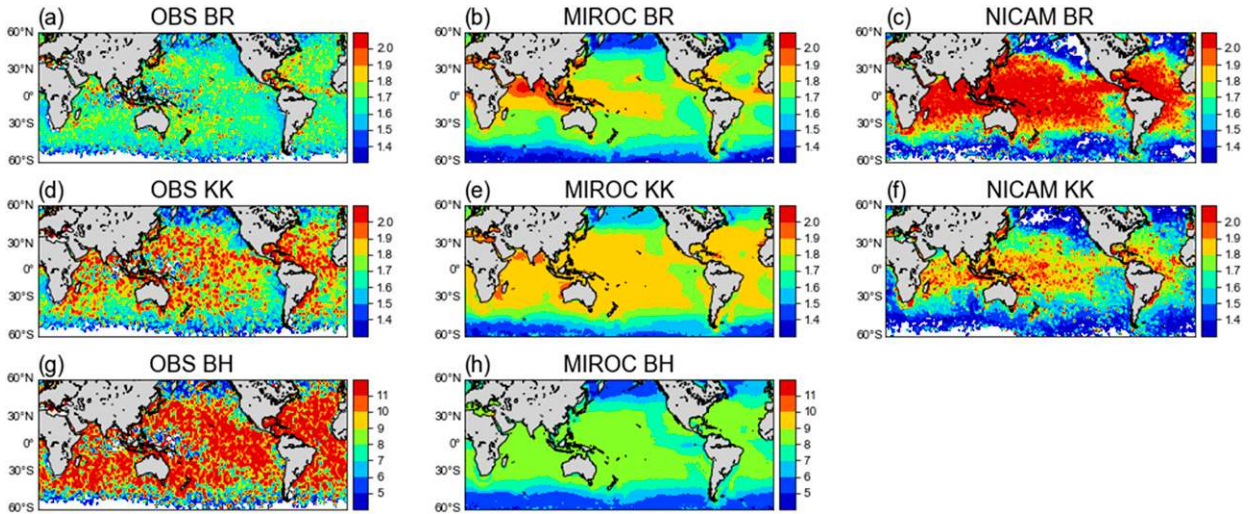


FIG. 6. Mean value of the factor E_{au} obtained from (left) satellite observations, (center) MIROC6, and (right) NICAM for the (a)–(c) BR, (d)–(f) KK, and (g), (h) BH autoconversion schemes.

SWCRE biases over the tropical open ocean regions in the Cont experiments (Figs. 8b,e,h) tend to be mitigated (Figs. 8d,g,j) as a consequence of latitudinal changes of LWP and CF. It is therefore reasonable to conclude that

incorporation of E_{au} with realistic regional distribution is useful to reduce the SWCRE biases in GCMs because E_{au} generally takes high values in tropical oceans (Fig. 6), where state-of-the-art GCMs typically

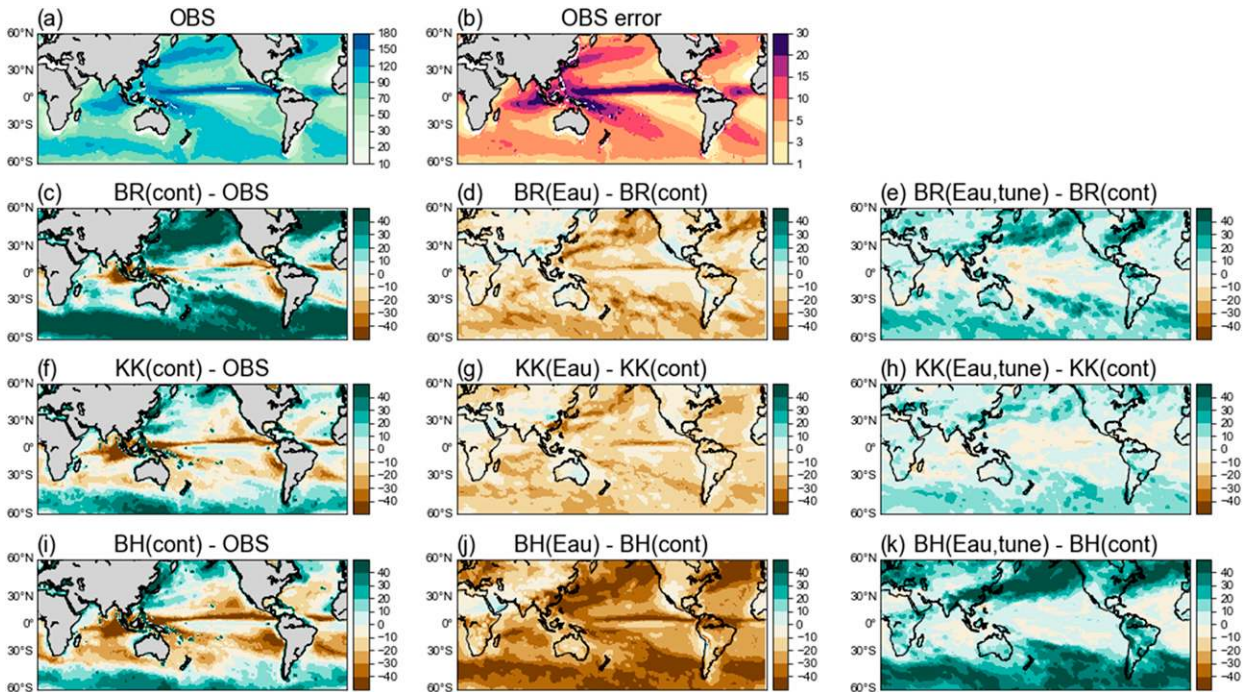


FIG. 7. Global climatology of (a) oceanic LWP (g m^{-2}) and (b) root-mean-square error of LWP (g m^{-2}) only for non-precipitating water from MAC-LWP for the years 2007–10. The data for (a) and (b) exclude rainwater from total (cloud and rain) water path (Elsaesser et al. 2017). Also shown are (c), (f), (i) the LWP bias of the MIROC6 Cont experiments and the LWP changes of the (d), (g), (j) E_{au} and (e), (h), (k) E_{au} -tune experiments relative to Cont experiments for the (second row) BR, (third row) KK, and (fourth row) BH autoconversion schemes. For MIROC6 LWP evaluation in (c)–(k), vertically integrated cloud water q_c is plotted and rainwater is not contained for the equivalent comparison to the MAC-LWP dataset.

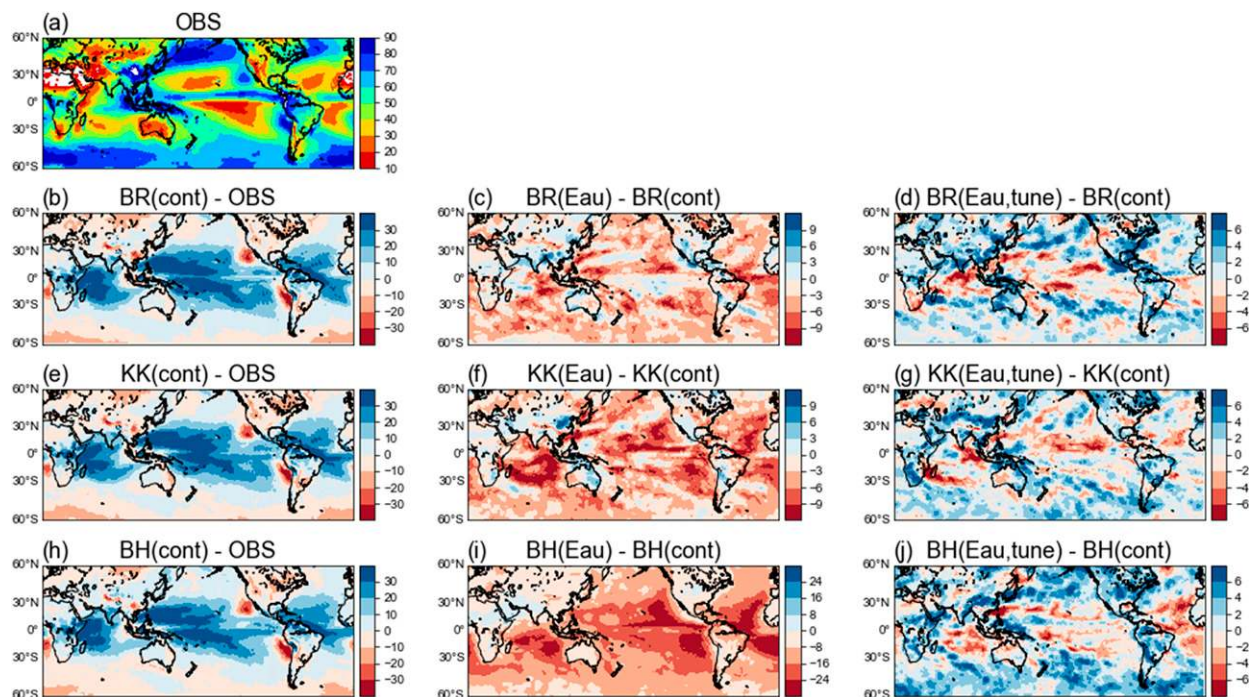


FIG. 8. (a) Global climatology of cloud radiative effect for outgoing shortwave radiation (SWCRE; W m^{-2}) at TOA from the observation of CERES-EBAF monthly data at 1° longitude and 1° latitude resolution over the 2006–10 period, and (b), (e), (h) the SWCRE bias of the MIROC6 Cont experiments and the SWCRE changes of the (c), (f), (i) MIROC6 E_{au} and (d), (g), (j) MIROC6 $E_{\text{au-tune}}$ experiments relative to Cont experiments for the (second row) BR, (third row) KK, and (fourth row) BH autoconversion schemes.

suffer from the too-reflective SWCRE biases (Nam et al. 2012; Lauer and Hamilton 2013). The tension between the LWP and SWCRE biases revealed should be addressed in the future.

d. Impact of enhancement factor on rain formation process

Since autoconversion is a key process determining the warm rain characteristics in models, E_{au} is also expected to influence the warm rain formation process. In particular, multiple GCMs are known to have too frequent and too light rain production as a common bias (Jing et al. 2017; Stephens et al. 2010; Suzuki et al. 2015). This bias is likely related to model representation of E_{au} , given that precipitation characteristics tend to be correlated with cloud inhomogeneity according to observational (Lebsock et al. 2013; Wu et al. 2018) and modeling (Takahashi et al. 2017) studies. Previous studies indeed showed that incorporation of E_{au} into GCMs changed the properties of rain production (Song et al. 2018a; Weber and Quaas 2012).

These arguments motivate us to investigate how cloud inhomogeneity and the resultant E_{au} relate to rain formation processes in MIROC6 in comparison to satellite observations and NICAM to specify the cause of precipitation biases attributable to cloud inhomogeneity

representation. For this purpose, warm clouds were grouped into three categories according to the column maximum of radar reflectivity, Ze_{max} : nonprecipitating, drizzling, and raining. MIROC6 analysis in this section was limited to the stratiform cloud subcolumns that adopt autoconversion and PDF parameterizations. Excluding convective cloud subcolumns from analysis had a negligible impact (not shown).

Figure 9 compares the V –CF relationships as in Fig. 2, but broken down into the three precipitation categories. Satellite observations (Fig. 9a) show that higher and lower V is associated with raining and nonprecipitating clouds, respectively, consistent with the previous studies (Lebsock et al. 2013; Takahashi et al. 2017). This suggests that cloud inhomogeneity plays an important role in the warm rain onset. NICAM qualitatively reproduces this dependence of V on precipitation state. In MIROC6, however, V is not appropriately related to the precipitation state. This is caused by the subgrid-scale cloud parameterization in MIROC6 based on the skewed-triangle PDF that binds E_{au} with CF too strongly. The cloud inhomogeneity and thus the E_{au} parameterization based solely on CF (Boutle et al. 2014) would fail to capture the observed dependence on precipitation. Instead, the Boutle et al. (2014) parameterization places this subgrid-scale dependence in the

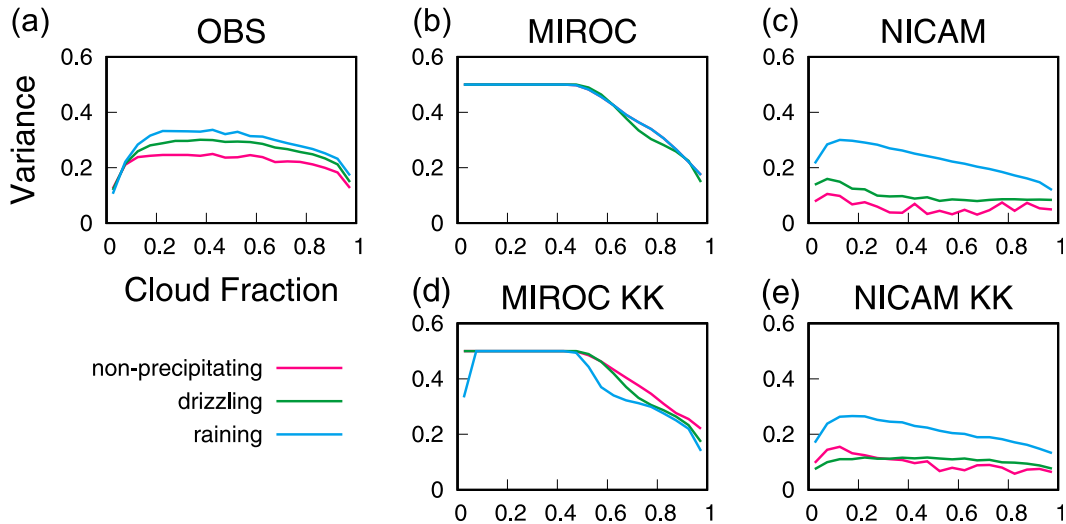


FIG. 9. The median value of cloud water normalized variance V for warm clouds (a) in satellite observations, in the MIROC6 E_{au} -tune experiments for the (b) BR and (d) KK autoconversion schemes, and in NICAM for the (c) BR and (e) KK autoconversion schemes. The precipitation state is categorized by the maximum Z_e within the cloud as non-precipitating ($Z_{e_max} < -15$ dBZ; magenta), drizzling (-15 dBZ $< Z_{e_max} < 0$ dBZ; green), and raining (0 dBZ $< Z_{e_max}$; light blue). Satellite statistics are constructed for a 4-yr period from 2007 to 2010 while the analysis for NICAM and MIROC6 is obtained from 2-month period (January and July in 2007) data with 6-hourly output.

accretion enhancement factor. Our work suggests that a dependence on precipitation is also present in E_{au} .

While the cloud inhomogeneity affects the precipitation process, the rain formation in turn modifies the cloud water distribution and cloudiness. Figure 10 compares the PDF of CF among different precipitation categories to investigate how the CF varies with precipitation characteristics.

Satellite observations show that raining clouds tend to be associated with small CF, suggesting that rain production depletes cloudiness. While NICAM qualitatively captures such a relationship, MIROC6 does not reproduce the observed relationship. This indicates that the MIROC6 PDF parameterization (Watanabe et al. 2009), in which the rain production modifies the total water PDF through the

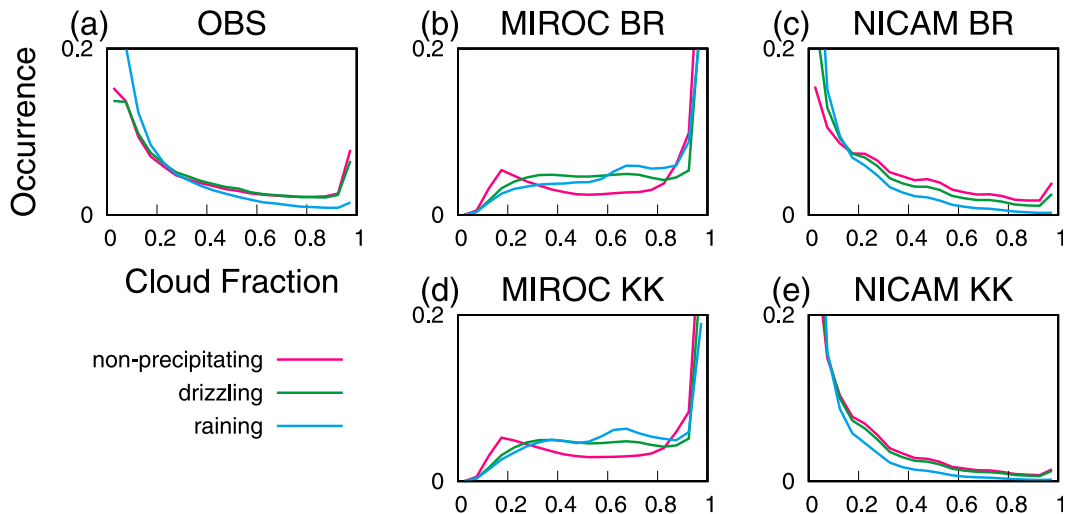


FIG. 10. PDF of cloud fraction (CF) with 0.05-width bin for three precipitation categories (non-precipitation in magenta; drizzling in green; and raining in light blue) (a) from satellite observations, from MIROC6 E_{au} -tune experiments for the (b) BR and (d) KK autoconversion schemes, and from NICAM for the (c) BR and (e) KK autoconversion schemes. Satellite statistics are constructed for the 4-yr period from 2007 to 2010 while the analysis for NICAM and MIROC6 is obtained from a 2-month period (January and July in 2007) of 6-hourly data output.

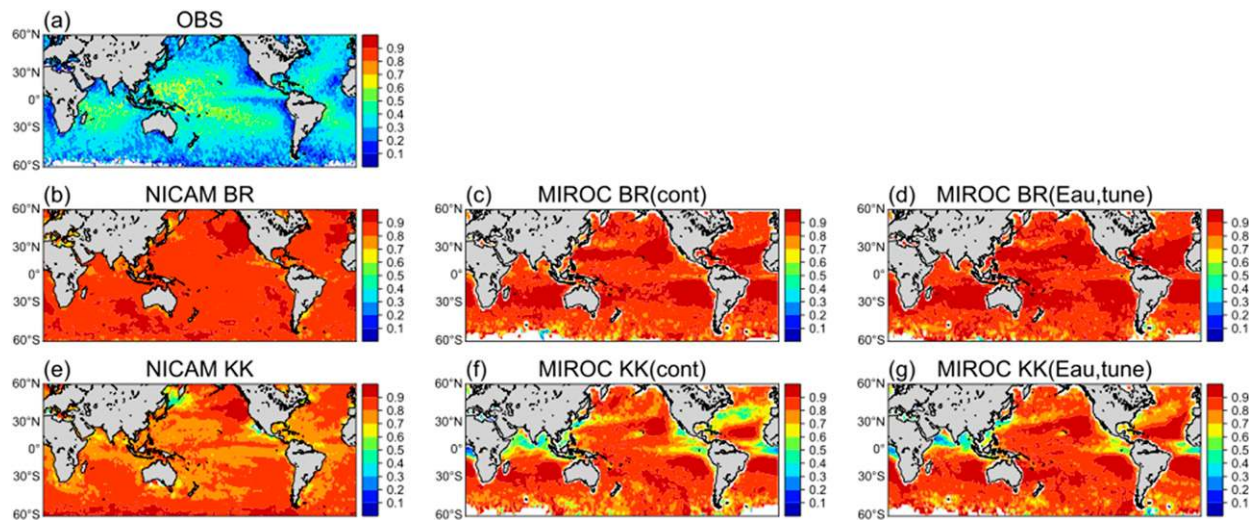


FIG. 11. Geographical distributions of the probability of precipitation (POP) for warm clouds from (a) satellite observations, (b),(e) NICAM, and (c),(d),(f),(g) MIROC6. POP is computed as a fractional occurrence of the precipitating category ($-15 \text{ dBZ} < Z_{e_max}$) relative to the total occurrence of warm clouds. Satellite statistics are constructed for the 4-yr period from 2007 to 2010 while the analysis for NICAM and MIROC6 is obtained from 2-month period (January and July in 2007) data of every 6-hourly output. The data were accumulated within the horizontal grids in MIROC6 and for $1.5^\circ \times 1.5^\circ$ grid in satellite observations and NICAM. To assess the overall climatic impact of E_{au} in MIROC6, the (center) Cont and (right) E_{au} -tune experiments are compared.

decrease of cloud water content, does not adequately relate the rain production to the cloud inhomogeneity.

Given these characteristics of E_{au} associated with precipitation, let us investigate whether the E_{au} might help mitigate the model biases in the rain formation. For this purpose, the probability of precipitation (POP) is compared in Fig. 11. The satellite analysis (Fig. 11a) suggests that a majority of the warm clouds are non-precipitating, particularly over subtropical eastern and midlatitude oceans, where E_{au} is relatively small (Fig. 6). Compared to satellite observations, POPs in the Cont experiments with both NICAM (Figs. 11b,e) and MIROC6 (Figs. 11c,f) are substantially higher, indicating that the precipitation occurs too frequently in the two models. Although the assumptions in satellite simulators [sections 2d and 3b(1)] might cause the too large radar reflectivity in the models, Jing et al. (2017) showed that assumption of rain fraction in COSP for MIROC6 or the relatively coarse resolution of J-simulator for NICAM do not explain all of the model–observation discrepancy. Despite the explicit representations of clouds in NICAM, POP is still too high and its observed geographical distribution is not reproduced in the model as also found in Suzuki et al. (2011). Also notable is that no significant effect of E_{au} on the POP is found in the E_{au} -tune experiment with MIROC6 (Figs. 11d,g), as opposed to previous GCM studies (Song et al. 2018a; Weber and Quaas 2012). This insensitivity of POP to E_{au} appears to be due to the constraints imposed by the PDF assumption, which prevents E_{au} from

representing the coupling between cloud inhomogeneity and precipitation formation (Figs. 6, 9, and 10).

It is thus suggested that E_{au} alone is not enough to mitigate the bias in MIROC6, particularly when the model retuning is applied to autoconversion only. The bias can be attributed, in part, to much larger autoconversion rate than accretion rate in the MIROC6 Cont experiments, which has not significantly changed with the introduction of E_{au} -tune alone (not shown). However, other possible improvements of model cloud physics, such as introducing the enhancement factor for accretion rate (Lebsock et al. 2013) and incorporating the prognostic treatment of rainwater (Michibata et al. 2019), can help achieve the proper balance of the process rates with smaller autoconversion rate and larger accretion rate. The model-simulated POPs are also dependent on microphysics such as choice of the autoconversion scheme (Jing et al. 2019; Suzuki et al. 2015) as indicated by POPs in the KK experiments somewhat lower and closer to satellite observation than in the BR case.

e. Implications for functional form of cloud water PDF

The results above show that the peculiarity inherent to MIROC6 PDF shape (i.e., a truncated skewed triangle) could be a possible source of bias in representing cloud inhomogeneity characteristics (Figs. 2, 4, 5, 9). In this regard, it is worth noting that previous studies adopted varying assumptions for $P(L_c)$: Some studies employed lognormal or gamma functions for $P(L_c)$ (Lebsock et al. 2013; Morrison and Gettelman 2008; Wu et al. 2018),

while others used the saturated part of $G(s)$ as $P(L_c)$, where $G(s)$ is assumed to be a variety of mathematical functions (Tompkins 2005). Here we discuss how behaviors of E_{au} tend to differ with varying assumptions of the PDF shape so that the results from the MIROC6 development described above can be put into the context of implications for other GCMs as well.

The theoretical relationships between V and S when $P(L_c)$ is assumed to be the lognormal and gamma functions are superimposed on Fig. 4a following Huang et al. (2014). These functions have been widely used for their convenience of allowing the enhancement factor for a power-law process to be obtained analytically. It is illustrated in Fig. 4a that both functions can capture the observed positive correlations between V and S with no definite value bounds and thus are able to represent the convective cloud PDF characterized by highly positively skewed distribution (Figs. 4e,f) with high value of E_{au} in contrast to the truncated skewed triangle in MIROC6 (Fig. 4d). Furthermore, these parameterizations allow cloud inhomogeneity to be free from CF and to be properly connected to precipitation processes as opposed to the truncated skewed triangle (Fig. 9). Such a sophisticated $P(L_c)$ assumption is, however, often inconsistent with the total water PDF assumption in GCMs (Guo et al. 2014; Song et al. 2018a).

For application to GCM cloud parameterizations, the characteristics of mathematical form for $G(s)$ would be even more important. Kawai and Teixeira (2012) showed that typical unimodal PDFs commonly result in the monotonic decrease of V with increasing CF (see Fig. 0.5a of Kawai and Teixeira 2012). On the one hand, this characteristic of V is preferable because V is expected to reproduce the geographical characteristics relevant to cloud regimes as long as CF distribution is realistic in the model (Figs. 2 and 3), which can help mitigate the too-reflective cloud bias at tropical oceans through E_{au} as discussed in section 4c. On the other hand, it was also shown that simple mathematical functions such as triangle and uniform with no or one prognostic parameter inherently fix the value of V at small CF similar to MIROC6 (Figs. 2, 9). This suggests that more sophisticated functions such as double-Gaussian and beta distributions (Larson and Golaz 2005; Tompkins 2002) need to be employed as $G(s)$ to better reproduce the observed bell-shaped relationship (Fig. 2) and the cloud inhomogeneity characteristics relevant to precipitation states (Fig. 9).

5. Summary

In this study, we have incorporated the enhancement factor for autoconversion process, E_{au} , into the MIROC6

GCM. The truncated part of prognostic skewed-triangle total water PDF is employed as cloud water PDF. The cloud water inhomogeneity and E_{au} thus implemented were evaluated against those simulated by the global high-resolution model, NICAM, with explicit representations of subgrid-scale cloud processes and those obtained from analysis of global satellite observations. It is found that large values of subgrid cloud variance V tend to be associated with small CF through the PDF assumption in MIROC6, which is qualitatively consistent with those found in NICAM and satellite observations (Fig. 2). This relationship regulates regional characteristics of E_{au} in MIROC6, which qualitatively reproduce the satellite-observed latitudinal variation of E_{au} (Fig. 6). The skewed-triangle PDF assumption of the MIROC6 cloud scheme, however, is also found to impose a strong constraint on E_{au} , which is overly constrained by CF and is restricted to unrealistically narrow ranges of value (Figs. 2, 4, 5). Such constraints manifest themselves as the absence of particularly large E_{au} at tropical convective cloud region (Fig. 6).

The global climate impact of E_{au} was then investigated using the MIROC6 experiments with and without E_{au} . The E_{au} -tune experiments, as clarified in the BH scheme case with the most intense magnitude of E_{au} , systematically increase (decrease) LWP and CF at low (high) latitudes over ocean (Fig. 7). As a result, the latitudinal variation of E_{au} , validated against NICAM and satellite observation, is shown to help reduce the too-reflective SWCRE bias over the tropical oceans (Fig. 8) typical of multiple GCMs. This suggests that the insufficient representation of cloud inhomogeneity might be a cause of the cloud biases commonly found in GCMs.

A possible linkage between the cloud inhomogeneity and the rain formation characteristics through E_{au} was also investigated. The PDF-based cloud scheme adopted by MIROC6 does not reasonably represent the observed linkage (Figs. 9, 10). Furthermore, no significant impact is found on the precipitation occurrence bias through the introduction of E_{au} in MIROC6 (Fig. 11), arguably due to the strong restriction on the E_{au} implemented. It is thus recommended that E_{au} be parameterized in such a way that E_{au} depends on precipitation states as well as cloud fraction.

The cloud inhomogeneity investigation is extended to a variety of PDFs to obtain implications for other GCMs as well. The results suggest that lognormal and gamma distributions are recommended for $P(L_c)$ given that these mathematical functions are able to roughly capture the observed cloud inhomogeneity correlations and can represent a wider range of V less bounded to CF (Fig. 4a). It is also found that V based on total water PDF generally decreased with increasing CF. The MIROC6

analysis has shown that this relationship forms the high E_{au} at small CF regions such as tropical ocean (Figs. 6a,d,g), which reduced shortwave reflection by clouds (Figs. 8d,g,j). Given that GCMs typically suffer from too-reflective cloud bias at tropical oceans, it is recommended to implement E_{au} based on the total water PDF in other GCMs as well.

The present study, taking E_{au} as an example, demonstrates how satellite observations and global high-resolution modeling can be jointly employed with global climate modeling to evaluate and constrain the unresolved subgrid cloud variability and explore its macroscopic climatic impact. The approach described would be applicable to other climate models as well to better characterize the multiple model biases and their causes attributable to coarse resolution and to investigate in what way the subgrid-scale parameterizations are useful to overcome such obstacles in climate modeling.

Acknowledgments. Simulations using MIROC6 were executed with the SX-9/ACE supercomputer system of the National Institute for Environmental Studies, Japan. This study was supported by the Integrated Research Program for Advancing Climate Models (TOUGOU program) Grant JPMXD0717935457 from the Ministry of Education, Culture, Sports, Science and Technology (MEXT), JAXA/GCOM-C, JAXA/EarthCARE projects, HPCI (hp180012, hp180181, and hp190151), and JSPS KAKENHI Grants (19H05669 and 19H05699). Matthew Lebsock's work was carried out at the Jet Propulsion Laboratory, California Institute of Technology, under contract with the National Aeronautics and Space Administration. The authors are grateful to three anonymous reviewers for providing insightful comments that helped to improve the manuscript.

REFERENCES

- Abdul-Razzak, H., and S. J. Ghan, 2000: A parameterization of aerosol activation: 2. Multiple aerosol types. *J. Geophys. Res.*, **105**, 6837–6844, <https://doi.org/10.1029/1999JD901161>.
- Ahlgrimm, M., and R. M. Forbes, 2016: Regime dependence of cloud condensate variability observed at the Atmospheric Radiation Measurement sites. *Quart. J. Roy. Meteor. Soc.*, **142**, 1605–1617, <https://doi.org/10.1002/qj.2783>.
- Barker, H., B. A. Weillick, and L. Parker, 1996: A parameterization for computing grid-averaged solar fluxes for inhomogeneous marine boundary layer clouds. Part II: Validation using satellite data. *J. Atmos. Sci.*, **53**, 2304–2316, [https://doi.org/10.1175/1520-0469\(1996\)053<2304:APFCGA>2.0.CO;2](https://doi.org/10.1175/1520-0469(1996)053<2304:APFCGA>2.0.CO;2).
- Beheng, K. D., 1994: A parameterization of warm cloud microphysical conversion processes. *Atmos. Res.*, **33**, 193–206, [https://doi.org/10.1016/0169-8095\(94\)90020-5](https://doi.org/10.1016/0169-8095(94)90020-5).
- Berry, E. X., 1968: Modification of the warm rain process. *Proc. First Conf. on Weather Modification*, Albany, NY, Amer. Meteor. Soc., 81–85.
- Bodas-Salcedo, A., and Coauthors, 2011: COSP: Satellite simulation software for model assessment. *Bull. Amer. Meteor. Soc.*, **92**, 1023–1043, <https://doi.org/10.1175/2011BAMS2856.1>.
- Boucher, O., and Coauthors, 2013: Clouds and aerosols. *Climate Change 2013: The Physical Science Basis*, T. F. Stocker et al., Eds., Cambridge University Press, 571–657.
- Boutle, I. A., S. J. Abel, P. G. Hill, and C. J. Morcrette, 2014: Spatial variability of liquid cloud and rain: Observations and microphysical effects. *Quart. J. Roy. Meteor. Soc.*, **140**, 583–594, <https://doi.org/10.1002/qj.2140>.
- Chepfer, H., S. Bony, D. Winker, M. Chiriaco, J.-L. Dufresne, and G. Sèze, 2008: Use of CALIPSO lidar observations to evaluate the cloudiness simulated by a climate model. *Geophys. Res. Lett.*, **35**, L15704, <https://doi.org/10.1029/2008GL034207>.
- , —, —, G. Cesana, J. L. Dufresne, P. Minnis, C. J. Stubenrauch, and S. Zeng, 2010: The GCM-oriented CALIPSO cloud product (CALIPSO-GOCCP). *J. Geophys. Res.*, **115**, D00H16, <https://doi.org/10.1029/2009JD012251>.
- Elsaesser, G. S., C. W. O'Dell, M. D. Lebsock, R. Bennartz, T. J. Greenwald, and F. J. Wentz, 2017: The Multisensor Advanced Climatology of Liquid Water Path (MAC-LWP). *J. Climate*, **30**, 10 193–10 210, <https://doi.org/10.1175/JCLI-D-16-0902.1>.
- Guo, H., J.-C. Golaz, L. J. Donner, P. Ginoux, and R. S. Hemler, 2014: Multivariate probability density functions with dynamics in the GFDL atmospheric general circulation model: Global tests. *J. Climate*, **27**, 2087–2108, <https://doi.org/10.1175/JCLI-D-13-00347.1>.
- Guzman, R., and Coauthors, 2017: Direct atmosphere opacity observations from CALIPSO provide new constraints on cloud-radiation interactions. *J. Geophys. Res. Atmos.*, **122**, 1066–1085, <https://doi.org/10.1002/2016JD025946>.
- Hashino, T., M. Satoh, Y. Hagihara, T. Kubota, T. Matsui, T. Nasuno, and H. Okamoto, 2013: Evaluating cloud microphysics from NICAM against CloudSat and CALIPSO. *J. Geophys. Res. Atmos.*, **118**, 7273–7292, <https://doi.org/10.1002/JGRD.50564>.
- Haynes, J. M., R. T. Marchand, Z. Luo, A. Bodas-Salcedo, and G. L. Stephens, 2007: A multipurpose radar simulation package: Quickbeam. *Bull. Amer. Meteor. Soc.*, **88**, 1723–1728, <https://doi.org/10.1175/BAMS-88-11-1723>.
- Hill, P. G., R. J. Hogan, J. Manners, and J. C. Petch, 2012: Parametrizing the horizontal inhomogeneity of ice water content using CloudSat data products. *Quart. J. Roy. Meteor. Soc.*, **138**, 1784–1793, <https://doi.org/10.1002/qj.1893>.
- , C. J. Morcrette, and I. A. Boutle, 2015: A regime-dependent parametrization of subgrid-scale cloud water content variability. *Quart. J. Roy. Meteor. Soc.*, **141**, 1975–1986, <https://doi.org/10.1002/qj.2506>.
- Hillman, B. R., R. T. Marchand, and T. P. Ackerman, 2018: Sensitivities of simulated satellite views of clouds to subgrid-scale overlap and condensate heterogeneity. *J. Geophys. Res. Atmos.*, **123**, 7506–7529, <https://doi.org/10.1029/2017JD027680>.
- Huang, D., E. Campos, and Y. Liu, 2014: Statistical characteristics of cloud variability. Part I: Retrieved cloud liquid water path at three ARM sites. *J. Geophys. Res. Atmos.*, **119**, 10 813–10 828, <https://doi.org/10.1002/2014JD022001>.
- Jing, X., K. Suzuki, H. Guo, D. Goto, T. Ogura, T. Koshiro, and J. Mülmenstädt, 2017: A multimodel study on warm precipitation biases in global models compared to satellite observations. *J. Geophys. Res. Atmos.*, **122**, 11 806–11 824, <https://doi.org/10.1002/2017JD027310>.
- , —, and T. Michibata, 2019: The key role of warm rain parameterization in determining the aerosol indirect effect in a global climate model. *J. Climate*, **32**, 4409–4430, <https://doi.org/10.1175/JCLI-D-18-0789.1>.

- Kawai, H., and J. Teixeira, 2012: Probability density functions of liquid water path and total water content of marine boundary layer clouds: Implications for cloud parameterization. *J. Climate*, **25**, 2162–2177, <https://doi.org/10.1175/JCLI-D-11-00117.1>.
- Kay, J. E., and Coauthors, 2012: Exposing global cloud biases in the Community Atmosphere Model (CAM) using satellite observations and their corresponding instrument simulators. *J. Climate*, **25**, 5190–5207, <https://doi.org/10.1175/JCLI-D-11-00469.1>.
- Khairoutdinov, M., and Y. Kogan, 2000: A new cloud physics parameterization in a large-eddy simulation model of marine stratocumulus. *Mon. Wea. Rev.*, **128**, 229–243, [https://doi.org/10.1175/1520-0493\(2000\)128<0229:ANCPPI>2.0.CO;2](https://doi.org/10.1175/1520-0493(2000)128<0229:ANCPPI>2.0.CO;2).
- Kodama, C., and Coauthors, 2015: A 20-year climatology of a NICAM AMIP-type simulation. *J. Meteor. Soc. Japan*, **93**, 393–424, <https://doi.org/10.2151/jmsj.2015-024>.
- Larson, V. E., and J.-C. Golaz, 2005: Using probability density functions to derive consistent closure relationships among higher-order moments. *Mon. Wea. Rev.*, **133**, 1023–1042, <https://doi.org/10.1175/MWR2902.1>.
- , R. Wood, P. R. Field, J.-C. Golaz, T. H. Vonder Haar, and W. R. Cotton, 2001: Systematic biases in the microphysics and thermodynamics of numerical models that ignore subgrid-scale variability. *J. Atmos. Sci.*, **58**, 1117–1128, [https://doi.org/10.1175/1520-0469\(2001\)058<1117:SBITMA>2.0.CO;2](https://doi.org/10.1175/1520-0469(2001)058<1117:SBITMA>2.0.CO;2).
- Lauer, A., and K. Hamilton, 2013: Simulating clouds with global climate models: A comparison of CMIP5 results with CMIP3 and satellite data. *J. Climate*, **26**, 3823–3845, <https://doi.org/10.1175/JCLI-D-12-00451.1>.
- Lebsock, M., H. Morrison, and A. Gettelman, 2013: Microphysical implications of cloud-precipitation covariance derived from satellite remote sensing. *J. Geophys. Res. Atmos.*, **118**, 6521–6533, <https://doi.org/10.1002/JGRD.50347>.
- Liu, Y., and P. H. Daum, 2004: Parameterization of the autoconversion process. Part I: Analytical formulation of the Kessler-type parameterizations. *J. Atmos. Sci.*, **61**, 1539–1548, [https://doi.org/10.1175/1520-0469\(2004\)061<1539:POTAPI>2.0.CO;2](https://doi.org/10.1175/1520-0469(2004)061<1539:POTAPI>2.0.CO;2).
- Loeb, N. G., and Coauthors, 2018: Clouds and the Earth's Radiant Energy System (CERES) Energy Balanced and Filled (EBAF) top-of-atmosphere (TOA) edition 4.0 data product. *J. Climate*, **31**, 895–918, <https://doi.org/10.1175/JCLI-D-17-0208.1>.
- Mace, G. G., Q. Zhang, M. Vaughan, R. Marchand, G. Stephens, C. Trepte, and D. Winker, 2009: A description of hydrometeor layer occurrence statistics derived from the first year of merged Cloudsat and CALIPSO data. *J. Geophys. Res.*, **114**, D00A26, <https://doi.org/10.1029/2007JD009755>.
- Michibata, T., and T. Takemura, 2015: Evaluation of autoconversion schemes in a single model framework with satellite observations. *J. Geophys. Res. Atmos.*, **120**, 9570–9590, <https://doi.org/10.1002/2015JD023818>.
- , K. Suzuki, M. Sekiguchi, and T. Takemura, 2019: Prognostic precipitation in the MIROC6-SPRINTARS GCM: Description and evaluation against satellite observations. *J. Adv. Model. Earth Syst.*, **11**, 839–860, <https://doi.org/10.1029/2018MS001596>.
- Morrison, H., and A. Gettelman, 2008: A new two-moment bulk stratiform cloud microphysics scheme in the Community Atmosphere Model, version 3 (CAM3). Part I: Description and numerical tests. *J. Climate*, **21**, 3642–3659, <https://doi.org/10.1175/2008JCLI2105.1>.
- Nam, C., S. Bony, J.-L. Dufresne, and H. Chepfer, 2012: The too few, too bright tropical low-cloud problem in CMIP5 models. *Geophys. Res. Lett.*, **39**, L21801, <https://doi.org/10.1029/2012GL053421>.
- Ogura, T., and Coauthors, 2017: Effectiveness and limitations of parameter tuning in reducing biases of top-of-atmosphere radiation and clouds in MIROC version 5. *Geosci. Model Dev.*, **10**, 4647–4664, <https://doi.org/10.5194/gmd-10-4647-2017>.
- Pincus, R., and S. A. Klein, 2000: Unresolved spatial variability and microphysical process rates in large-scale models. *J. Geophys. Res.*, **105**, 27 059–27 065, <https://doi.org/10.1029/2000JD900504>.
- Platnick, S., M. D. King, S. A. Ackerman, W. P. Menzel, B. A. Baum, J. C. Riédi, and R. A. Frey, 2003: The MODIS cloud products: Algorithms and examples from Terra. *IEEE Trans. Geosci. Remote Sens.*, **41**, 459–473, <https://doi.org/10.1109/TGRS.2002.808301>.
- Rotstayn, L. D., 2000: On the “tuning” of autoconversion parameterizations in climate models. *J. Geophys. Res.*, **105**, 15 495–15 507, <https://doi.org/10.1029/2000JD900129>.
- Sato, Y., D. Goto, T. Michibata, K. Suzuki, T. Takemura, H. Tomita, and T. Nakajima, 2018: Aerosol effects on cloud water amounts were successfully simulated by a global cloud-system resolving model. *Nat. Commun.*, **9**, 985, <https://doi.org/10.1038/s41467-018-03379-6>.
- Satoh, M., T. Matsuno, H. Tomita, H. Miura, T. Nasuno, and S. Iga, 2008: Nonhydrostatic Icosahedral Atmospheric Model (NICAM) for global cloud resolving simulations. *J. Comput. Phys.*, **227**, 3486–3514, <https://doi.org/10.1016/j.jcp.2007.02.006>.
- , and Coauthors, 2014: The Non-hydrostatic Icosahedral Atmospheric Model: Description and development. *Prog. Earth Planet. Sci.*, **1**, 18, <https://doi.org/10.1186/s40645-014-0018-1>.
- , B. Stevens, F. Judt, M. Khairoutdinov, S.-J. Lin, W. M. Putman, and P. Düben, 2019: Global cloud-resolving models. *Curr. Climate Change Rep.*, **5**, 172–184, <https://doi.org/10.1007/s40641-019-00131-0>.
- Shonk, J., R. Hogan, J. Edwards, and G. Mace, 2010: Effect of improving representation of horizontal and vertical cloud structure on the Earth's global radiation budget. Part I: Review and parametrization. *Quart. J. Roy. Meteor. Soc.*, **136**, 1191–1204, <https://doi.org/10.1002/QJ.647>.
- Sommeria, G., and J. Deardorff, 1977: Subgrid-scale condensation in models of nonprecipitating clouds. *J. Atmos. Sci.*, **34**, 344–355, [https://doi.org/10.1175/1520-0469\(1977\)034<0344:SSCIMO>2.0.CO;2](https://doi.org/10.1175/1520-0469(1977)034<0344:SSCIMO>2.0.CO;2).
- Song, H., Z. Zhang, P.-L. Ma, S. J. Ghan, and M. Wang, 2018a: An evaluation of marine boundary layer cloud property simulations in the Community Atmosphere Model using satellite observations: Conventional subgrid parameterization versus CLUBB. *J. Climate*, **31**, 2299–2320, <https://doi.org/10.1175/JCLI-D-17-0277.1>.
- , —, —, S. Ghan, and M. Wang, 2018b: The importance of considering sub-grid cloud variability when using satellite observations to evaluate the cloud and precipitation simulations in climate models. *Geosci. Model Dev.*, **11**, 3147–3158, <https://doi.org/10.5194/gmd-11-3147-2018>.
- Stephens, G. L., 2005: Cloud feedbacks in the climate system: A critical review. *J. Climate*, **18**, 237–273, <https://doi.org/10.1175/JCLI-3243.1>.
- , and Coauthors, 2002: The CloudSat mission and the A-Train: A new dimension of space-based observations of clouds and precipitation. *Bull. Amer. Meteor. Soc.*, **83**, 1771–1790, <https://doi.org/10.1175/BAMS-83-12-1771>.
- , and Coauthors, 2008: CloudSat mission: Performance and early science after the first year of operation. *J. Geophys. Res.*, **114**, D00A18, <https://doi.org/10.1029/2008JD009982>.

- , and Coauthors, 2010: Dreary state of precipitation in global models. *J. Geophys. Res.*, **115**, D24211, <https://doi.org/10.1029/2010JD014532>.
- , D. Winker, J. Pelon, C. Trepte, D. Vane, C. Yuhas, T. L'Ecuyer, and M. Lebsock, 2018: CloudSat and CALIPSO within the A-Train: Ten years of actively observing the Earth system. *Bull. Amer. Meteor. Soc.*, **99**, 569–581, <https://doi.org/10.1175/BAMS-D-16-0324.1>.
- Suzuki, K., T. Nakajima, M. Satoh, H. Tomita, T. Takemura, T. Y. Nakajima, and G. L. Stephens, 2008: Global cloud-system-resolving simulation of aerosol effect on warm clouds. *Geophys. Res. Lett.*, **35**, L19817, <https://doi.org/10.1029/2008GL035449>.
- , G. L. Stephens, S. C. van den Heever, and T. Y. Nakajima, 2011: Diagnosis of the warm rain process in cloud-resolving models using joint CloudSat and MODIS observations. *J. Atmos. Sci.*, **68**, 2655–2670, <https://doi.org/10.1175/JAS-D-10-05026.1>.
- , J.-C. Golaz, and G. L. Stephens, 2013: Evaluating cloud tuning in a climate model with satellite observations. *Geophys. Res. Lett.*, **40**, 4464–4468, <https://doi.org/10.1002/grl.50874>.
- , G. L. Stephens, A. Bodas-Salcedo, M. Wang, J.-C. Golaz, T. Yokohata, and T. Koshiro, 2015: Evaluation of the warm rain formation process in global models with satellite observations. *J. Atmos. Sci.*, **72**, 3996–4014, <https://doi.org/10.1175/JAS-D-14-0265.1>.
- Takahashi, H., M. Lebsock, K. Suzuki, G. L. Stephens, and M. Wang, 2017: An investigation of microphysics and subgrid-scale variability in warm-rain clouds using the A-Train observations and a multiscale modeling framework. *J. Geophys. Res. Atmos.*, **122**, 7493–7504, <https://doi.org/10.1002/2016JD026404>.
- Takemura, T., T. Nozawa, S. Emori, T. Y. Nakajima, and T. Nakajima, 2005: Simulation of climate responses to aerosol direct and indirect effects with aerosol transport-radiation model. *J. Geophys. Res.*, **110**, D02202, <https://doi.org/10.1029/2004JD005029>.
- , M. Egashira, K. Matsuzawa, H. Ichijo, R. O'ishi, and A. Abe-Ouchi, 2009: A simulation of the global distribution and radiative forcing of soil dust aerosols at the last glacial maximum. *Atmos. Chem. Phys.*, **9**, 3061–3073, <https://doi.org/10.5194/ACP-9-3061-2009>.
- Tanelli, S., S. L. Durden, E. Im, K. S. Pak, D. G. Reinke, P. Partain, J. M. Haynes, and R. T. Marchand, 2008: CloudSat's cloud profiling radar after two years in orbit: Performance, calibration, and processing. *IEEE Trans. Geosci. Remote Sens.*, **46**, 3560–3573, <https://doi.org/10.1109/TGRS.2008.2002030>.
- Tatebe, H., and Coauthors, 2019: Description and basic evaluation of simulated mean state, internal variability, and climate sensitivity in MIROC6. *Geosci. Model Dev.*, **12**, 2727–2765, <https://doi.org/10.5194/gmd-12-2727-2019>.
- Tomita, H., 2008: New microphysical schemes with five and six categories by diagnostic generation of cloud ice. *J. Meteor. Soc. Japan*, **86A**, 121–142, <https://doi.org/10.2151/jmsj.86A.121>.
- , and M. Satoh, 2004: A new dynamical framework of non-hydrostatic global model using the icosahedral grid. *Fluid Dyn. Res.*, **34**, 357–400, <https://doi.org/10.1016/j.fluiddyn.2004.03.003>.
- Tompkins, A. M., 2002: A prognostic parameterization for the subgrid-scale variability of water vapor and clouds in large-scale models and its use to diagnose cloud cover. *J. Atmos. Sci.*, **59**, 1917–1942, [https://doi.org/10.1175/1520-0469\(2002\)059<1917:APPFTS>2.0.CO;2](https://doi.org/10.1175/1520-0469(2002)059<1917:APPFTS>2.0.CO;2).
- , 2005: The parametrization of cloud cover. ECMWF Moist Processes Lecture Note Series Tech. Memo., 25 pp.
- , 2008: Cloud parametrization. *Proc. ECMWF Seminar on Parametrization of Subgrid Physical Processes*, Reading, United Kingdom, ECMWF, 27–62, <http://www.ecmwf.int/publications/library/do/references/show?id=88790>.
- Tripoli, G., and W. Cotton, 1980: A numerical investigation of several factors contributing to the observed variable intensity of deep convection over south Florida. *J. Appl. Meteor.*, **19**, 1037–1063, [https://doi.org/10.1175/1520-0450\(1980\)019<1037:ANIOSF>2.0.CO;2](https://doi.org/10.1175/1520-0450(1980)019<1037:ANIOSF>2.0.CO;2).
- Watanabe, M., S. Emori, M. Satoh, and H. Miura, 2009: A PDF-based hybrid prognostic cloud scheme for general circulation models. *Climate Dyn.*, **33**, 795–816, <https://doi.org/10.1007/s00382-008-0489-0>.
- Weber, T., and J. Quaas, 2012: Incorporating the subgrid-scale variability of clouds in the autoconversion parameterization using a PDF-scheme. *J. Adv. Model. Earth Syst.*, **4**, M11003, <https://doi.org/10.1029/2012MS000156>.
- Wilson, D. R., and S. P. Ballard, 1999: A microphysically based precipitation scheme for the UK Meteorological Office Unified Model. *Quart. J. Roy. Meteor. Soc.*, **125**, 1607–1636, <https://doi.org/10.1002/qj.49712555707>.
- Wood, R., 2006: Relationships between optical depth, liquid water path, droplet concentration, and effective radius in adiabatic layer cloud. University of Washington Rep., 3 pp., https://atmos.uw.edu/~robwood/papers/chilean_plume/optical_depth_relations.pdf.
- Wu, P., B. Xi, X. Dong, and Z. Zhang, 2018: Evaluation of autoconversion and accretion enhancement factors in general circulation model warm-rain parameterizations using ground-based measurements over the Azores. *Atmos. Chem. Phys.*, **18**, 17 405–17 420, <https://doi.org/10.5194/acp-18-17405-2018>.
- Xie, X., and M. Zhang, 2015: Scale-aware parametrization of liquid cloud inhomogeneity and its impact on simulated climate in CESM. *J. Geophys. Res. Atmos.*, **120**, 8359–8371, <https://doi.org/10.1002/2015JD023565>.
- Zhang, M. H., and Coauthors, 2005: Comparing clouds and their seasonal variations in 10 atmospheric general circulation models with satellite measurements. *J. Geophys. Res.*, **110**, D15S02, <https://doi.org/10.1029/2005JD005923>.
- Zhang, Z., H. Song, P.-L. Ma, V. E. Larson, M. Wang, X. Dong, and J. Wang, 2019: Subgrid variations of the cloud water and droplet number concentration over tropical ocean: Satellite observations and implications for warm rain simulation in climate models. *Atmos. Chem. Phys.*, **19**, 1077–1096, <https://doi.org/10.5194/acp-19-1077-2019>.